*Journal of Applied Fluid Mechanics*, Vol. 16, No. 7, pp. 1356-1370, 2023.
Available online at www.jafmonline.net, ISSN 1735-3572, EISSN 1735-3645.
https://doi.org/10.47176/jafm.16.07.1539

# Performance Optimization of Nozzle-Diffuser Piezoelectric Micropump with Multiple Vibrating Membranes by Design of Experiment (DOE) Method

S. Bayazidi[1,2], M. Mojaddam[1] and A. Mohseni[1†]

[1] *Faculty of Mechanical and Energy Engineering, Shahid Beheshti University (SBU), Tehran, 1983969411, Iran*
[2] *Current Affiliation: School of Mechanical Engineering, Iran University of Science and Technology (IUST), Tehran, 1684613114, Iran*

†*Corresponding Author Email: ar_mohseni@sbu.ac.ir*

(Received August 29, 2022; accepted March 4, 2023)

## ABSTRACT

During recent years, microfluidics based microelectromechanical systems (MEMSs) have found multiple applications in biomedical engineering. One of their most important implementations is fluid transfer in microliter and nanoliter scales. Nowadays, micropumps are extensively used in various medical applications such as drug delivery. In this study, the performance of a piezoelectric micropump is investigated and optimized. This micropump consists of a pump chamber and three deformable walls in a nozzle-diffuser shape, which are used to create pressure gradient between the inlet and outlet. The performance of the micropump is evaluated by transient Computational Fluid Dynamics (CFD) simulation using dynamic mesh. Then its performance is optimized using the Design of Experiment (DOE) method based on mean net outlet mass flow rate and flow reversibility at the pump outlet. The results indicate an improvement of 34.5% in mean net outlet mass flow rate and a significant decrease in reversibility. The maximum mean net outlet mass flow rate and the minimum reversibility corresponding to the optimum geometries are 95.82 mL/min and 0.05%, respectively.

**Keywords**: Micropump; Piezoelectric; Microfluidics; Design of Experiment; Optimization.

## NOMENCLATURE

| | | | |
|---|---|---|---|
| $a_k$ | movement amplitude of the $k$th membrane | $t$ | time |
| $A$ | cross-sectional area | $T$ | time period |
| $b_k$ | intercept of the $k$th membrane | $u_k$ | $k$th velocity component of fluid |
| $D$ | chamber depth | $u_k^{PM}$ | $u_k$ in pump mode |
| $f_k$ | movement frequency of the $k$th membrane | $u_k^{SM}$ | $u_k$ in supply mode |
| $K$ | number of levels | $x_k$ | $k$th coordinate component |
| $L_k$ | length of the $k$th membrane | $Y_k$ | vertical position of the $k$th membrane |
| $\dot{m}$ | net mass flow rate | $\alpha, \beta$ | coefficients of Eq. (12) |
| $\overline{\dot{m}}$ | mean net mass flow rate | ȯ | regression error |
| $\dot{m}^+$ | forward mass flow rate | $\varepsilon$ | relative error |
| $\dot{m}^-$ | reverse mass flow rate | $\nu$ | kinematic viscosity of fluid |
| $\dot{m}^g$ | gross mass flow rate | $\rho$ | density of fluid |
| $m_k$ | slope of the $k$th membrane | $\varphi_{ex}$ | reverse mass flow rate ratio at micropump outlet |
| $n$ | number of geometric parameters | $\overline{\varphi}_{ex}$ | reversibility or mean reverse mass flow rate ratio at micropump outlet |
| $N$ | number of design points | | |
| $p$ | fluid pressure | | |

## 1. INTRODUCTION

In recent years, microfluidic systems including micropumps, microchannels, microvalves, micro-reactors, and micromixers have received widespread attention due to their applications in medicine, drug delivery, biology, pharmacy, cooling of electronic devices, chemical mixing and analysis, space explorations etc. (Verma *et al.* 2009; Kumar 2010; Karimi *et al.* 2021). The ability to pump fluids at low flow rates and in a controlled manner can for example help diabetic patients and patients with muscular contractions or chronic pain. The benefits of working with micro-scale fluid devices include considerable ease of handling and significant reductions in device sizes, manual interference, and costs (Iverson and Garimella 2008; Zahn 2015; Karimi *et al.* 2019; Noruz Shamsian *et al.* 2020). The possibility of pumping fluids in microliter and nanoliter volumes provides new basis for future applications in the medical and drug delivery fields.

Micropumps are commonly driven by piezoelectric, electrostatic, electromagnetic, electrohydrodynamic, or pneumatic actuators. Micropumps consume various forms of energy such as electrical and thermal to create volumetric pressure oscillations in a fluid (Saggere 2015).

Piezoelectric micropump is one of the most widely used type of micropump in drug delivery and other medical applications. The main characteristics of piezoelectric micropumps are high stimulation power, fast response, applicability in a wide frequency band, simple structure, satisfactory biocompatibility, small size, and cost effectiveness (Cui *et al*. 2008). High sensitivity of biological and pharmaceutical materials to temperature and chemical reactions is one of the main reasons for using piezoelectric micropumps in medical applications.

Extensive numerical and experimental studies have been conducted to find better intuitions regarding characteristics and requirements of micropump design in different applications. The first activities to manufacture micropump based microelectromechanical systems (MEMSs) began in the late 1980s (Yamahata *et al.* 2005). The first micropumps were made of silicon in micro scale, which subsequently drew a lot of attention due to their high capability of downsizing (Ohnstein *et al*. 1990; Shoji *et al*. 1990). Van Lintel et al. constructed the first pump with a micro-diaphragm and a one-way valve. The proposed reciprocal displacement micropumps consisted of a chamber, a thin membrane stimulated with a piezoelectric disk, and check valves to produce rectified flow (Abhari *et al*. 2012). Smiths proposed a peristaltic pump with three active valves which was stimulated with piezoelectric disks. His design was developed to control the delivery of insulin to body (Smits 1990).

The first micropump which did not use one-way valves was developed by Stemme, who used a nozzle and a diffuser for flow rectification (Stemme and Stemme 1993). Zhu *et al.* (2009) designed a plastic micropump with a metal diaphragm and three piezoelectric ceramics. By designing a simple actuated valve, this pump eliminated some of the disadvantages of regular valves.

Yao et al. simulated a three-dimensional transient flow in a valveless micropump. The results indicated that the maximum mass flow rate was achieved at a frequency of 200 Hz at zero differential pressure across the pump (Yao *et al*. 2007). Koombua et al. modeled two-dimensional fluid flow in a nozzle-diffuser micropump with vibrating membrane and piezoelectric actuator. The results indicated that the highest mass flow rate was obtained at the highest frequency and the maximum displacement of membrane wall (Koombua *et al*. 2008). Su and Pidaparti (2010) evaluated a nozzle-diffuser micropump without using valves to transmit biological materials. Both stimulus frequency and particle size had significant effects on the retention time and spatial distribution of transmitted particles from micropump. Sateesh *et al.* (2018) simulated fluid flow in a micropump with piezoelectric actuator and indicated that the optimum pump reached a maximum flow velocity of 0.039 μm/s for turbulent flow in the channel and reached 0.029 μm/s for laminar flow.

In another study, Piterah *et al*. (2017) proposed a valveless micropump design with reciprocating micropumping concept. This micropump was specifically designed to overcome hydrodynamic reverse flow at low Reynolds numbers. A valveless and vaneless piezoelectric pump as compared with pumps with moving parts, eliminates the risk of wear and fatigue in check valve and also reduces the danger of valve clogging.

With the availability and increase of computational power, design optimization has become an integrated step of most design procedures. Optimization techniques have been extensively used in the design of modern turbomachines (Li and Zheng 2017; Yazdani and Mohseni 2017; Namazizadeh *et al.* 2020). In comparison, however, the application of optimization techniques in micropump design is still at its early stage. There are several aspects of micropumps with complex dynamic behavior (Zengerle and Richter 1994), which reveal the importance and necessity of performance optimization. Given a pump that operates at an optimal condition, any deviation from optimal settings can cause reduction and possibly lack of performance. Considering the small sizes of micropumps, the relative effects of surface quality, manufacturing tolerances, dynamic behavior etc. are more prominent than regular pumps, which indicate high potential effectiveness of shape optimization in micropumps. Especially in micropumps which rely on dynamic fluid action, the performance and stability of pump is susceptible to temporal geometric features of flow passage.

This study investigates the performance of a valveless piezoelectric micropump consisting of a nozzle-diffuser-type chamber with three vibrating wall membranes by implementing CFD to investigate the transient behavior of the pump. The

focus is on the performance optimization of the micropump.

Contrary to the pumps with check valves, in which positive flow is enforced by valve action, in valveless micropumps the net mass flow rate of pump is a result of synchronous dynamic actions of flow driving parts, such as moving walls. A partial deviation from synchronous action may lead to partial counteraction of one or more parts, in which case the induced energy to fluid may serve to build resistance against the action of the other parts which are still working in a favorable mode. It is, therefore, important to study the sensitivity of micropump to its operation parameters and conditions and to determine the extent within which the pump maintains its optimal performance (Kim *et al.* 2005; He *et al.* 2017).

In order to optimize the performance of the micropump in this study, maximization of mean output mass flow rate, minimization of reversibility, and impact of geometrical configurations are investigated by changing the geometric parameters using the DOE method. Firstly the effects of different design parameters on the pump performance are recognized and quantified. Secondly the pump design is optimized. This pump can be used to transport viscous liquids such as biological materials (e.g. blood) and is suited for flexible and controlled drug delivery.

## 2. STRUCTURE AND OPERATION PRINCIPLE

The structure of the micropump, shown in Fig. 1, consists of a pump chamber with three vibrating nozzle-diffuser-type polymer membranes of Polydimethylsiloxane (PDMS) to create pressure difference and flow movement through the pump chamber, piezoelectric actuator on the membranes walls (a.k.a. side walls), and cover plates on top and bottom of the chamber. In order to study the dynamic action of the membranes, the effect of the top and bottom covers are excluded in this study. The movement of the membrane wall is achieved by the piezoelectric actuator and is precisely controlled by the applied electric power. For comparison and validation of the computations, the dimensions of the baseline pump are selected to match the reported dimensions in reference articles Koombua *et al.* (2008), Su and Pidaparti (2010), and Koombua and Pidaparti (2010). The micropump chambers C1, C2,

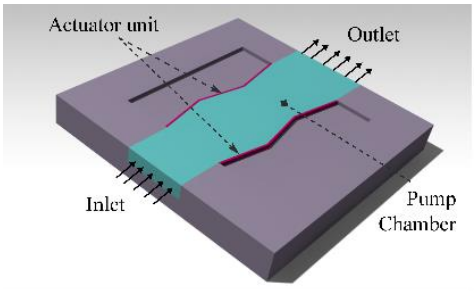


**Fig. 1. Structure of the micropump chamber with multiple vibrating membranes.**

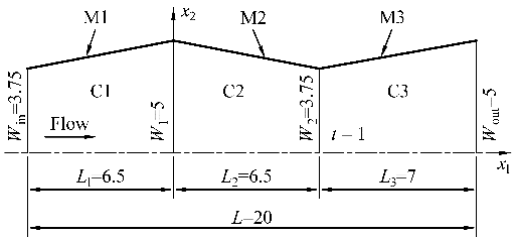


**Fig. 2. Upper half of the micropump chamber, piezoelectric membranes (M1, M2, M3), and main dimensions. Dimensions are in mm.**

and C3, membranes M1, M2, and M3, and the chamber dimensions are illustrated in Fig 2. $W_{in}$ is half of the inlet width, $W_{out}$ is half the output width, $W_1$ and $W_2$ are the half-width of the first and second throats, respectively, $L$ is the length of the pump, $L_1$, $L_2$, and $L_3$ are the axial lengths of chambers C1, C2, and C3, respectively, and $D$ is the chamber depth.

The deformation of the piezoelectric membranes causes the increase and decrease of the volume of the micropump chamber. In the following it will be shown that the dynamic deformation of membranes plays an important role in producing reversibility and inducing net mass flow.

Figure 3 illustrates the operation of the micropump in both pumping and supplying modes. In the pumping mode, Fig. 3a, membranes 1 and 2 move downward and membrane 3 moves upward causing to pump the fluid in the flow direction. As membranes 1 and 2 move downward, the volumes of chambers 1 and 2 decrease and pressure increases in these volumes. At the same time as membrane 3 moves upward, the volume of chamber 3 increases and its pressure decreases. Therefore, the inlet fluid moves from the high-pressure chambers 1 and 2 towards the low-pressure chamber 3 and discharges from the pump.

In supplying mode, Fig. 3b, membranes 1 and 2 move upward and membrane 3 moves downward. Hence, the pressure in chambers 1 and 2 decreases and the pressure of chamber 3 increases. As the

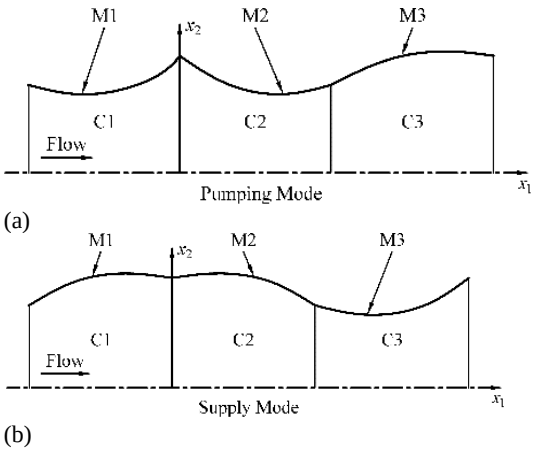


**Fig. 3. Operation of the micropump in, (a) pump mode, (b) supply mode. Only the upper half of the flow channel is illustrated.**

result, the fluid is sucked into the pump from the inlet while a minimum positive flow is maintained at the pump discharge or the back flow at the outlet into chamber 3 is minimized.

## 3. MODELING

### 3.1 Governing Equations

Laminar, incompressible, and isothermal flow of Newtonian fluid with constant properties are the simulation assumptions in this study. The governing equations include the continuity and momentum equations are as follows (Currie 2016).

$$u_{k,k} = 0 \tag{1}$$

$$u_{j,t} + u_k u_{j,k} = \frac{-1}{\rho} p_{,j} + [\nu(u_{k,j} + u_{j,k})]_{,j} \tag{2}$$

where $u_k$, $p$, $\rho$, and $\nu$ indicate velocity component, pressure, density, and kinematic viscosity of fluid, respectively. Indices following comma denote partial differentiation with respect to spatial coordinate components, e.g. for a typical function $\varphi(t, x_i)$, $\varphi_{,ij} \equiv \partial^2\varphi / \partial x_i \partial x_j$, except for $t$, which denotes temporal differentiation, e.g. $\varphi_{,t} \equiv \partial\varphi / \partial t$. The Einstein's summation convention for repeated indices is implied. The momentum equation (2) includes the transient terms to account for boundary movement.

### 3.2 Membrane Movement

Flow movement in the micropump is caused by the vibration of membranes. In this study it is assumed that the structure of the micropump is stiff enough that the interaction between the fluid and membranes does not affect the movement of membranes and, therefore, a one-way Fluid Structure Interaction (FSI) can be considered. The time-dependent movement of both of the side membrane walls is defined by the following equation (Su and Pidaparti 2010), which is an approximate model of membrane movement based on the first mode of vibration of a string hinged at both ends (Koombua *et al*. 2008).

$$Y_k(x_1, t) = b_k + m_k x_1 + a_k \sin\left(\frac{\pi x_1}{L_k}\right)\sin(2\pi f_k t) \tag{3}$$

In this equation, $Y_k$ is the displacement of the $k$th membrane, $k \in \{1,2,3\}$, in the $x_2$ direction, $x_1 \in [0, L_k]$ represents the longitudinal position of the membrane, $m_k$ is the slope of membrane $k$, $b_k$ is the intercept of membrane $k$ on the $x_2$ axis, $L_k$ indicates the length of membrane $k$, $a_k$ is the maximum displacement or amplitude, $f_k$ is the frequency of oscillation, and $t$ represents time. Eq. (3) defines an imposed movement model to the micropump using the first mode of vibration of the membranes. Although practically feasible, it is not meant to be the deformation model of a specific experimental realization of the micropump. This model provides the deformation space provided by the first mode of vibration of the membranes which also defines the search space for pump optimization process in this study. The configurations of the membranes are shown in Fig. 4.

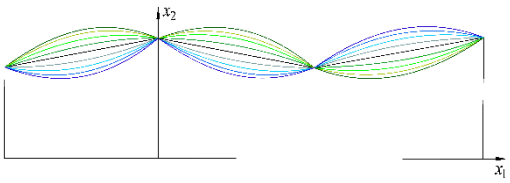


**Fig. 4. Configuration of the membranes.**

## 4. NUMERICAL SIMULATION OF FLOW FIELD

The flow in the pump channel is assumed in the $x_1x_2$ plane, and it is assumed that the side walls (membranes) move synchronously and have dynamic geometrical symmetry with respect to the $x_1$ axis. Also, it is assumed that fluid flow is symmetric with respect to the $x_1$-axis. Therefore, only the flow in the upper half of the channel is considered in the numerical simulation and the mean net outlet mas flow rate and reversibility are computed (Cui *et al.* 2008; Su and Pidaparti 2010).

To implement the movement of the membranes during the solution of the governing equations (1) and (2), boundary conditions and computational domain are updated at each time step. SIMPLE (Semi-Implicit Method for Pressure-Linked Equations) algorithm (Patankar and Spalding 1972) for steady state and PISO (Pressure Implicit with Splitting of Operators) algorithm (Issa 1986) for transient flow field are used to solve the velocity-pressure coupled equations. The working fluid in this study is water with a density of 998.2 kg/m$^3$ and a coefficient of dynamic viscosity of 0.001 kg/(m·s). The overall length of the micropump is 20 mm, the depth of the chamber is 1 mm, the inlet width of the micropump is 7.5 mm, and the outlet width is 10 mm. The movement amplitudes of all membranes $a_k$ and their frequencies $f_k$ are assumed to be 1 mm and 100 Hz, respectively.

As the micropump membranes vibrate, re-meshing of the computational domain is required after each time step. Therefore, dynamic meshing is used to simulate the transient flow field inside the micropump. In this article smoothing method was used to adjust mesh to deformed boundaries, which maintains the number of nodes and stretches the edges as in a set of interconnected springs (Yao *et al*. 2013).

At each time step the solution is considered converged, when the residual of continuity and momentum equations at steady-state simulation are less than $10^{-6}$ and $10^{-8}$, respectively, and for transient simulation are less than $10^{-6}$. In steady-state simulation, which is intended to investigate the fluid dynamics of the channel, a pressure difference

boundary condition of 0.0046 Pa between the inlet and outlet of the micropump is applied. The relative inlet stagnation pressure and outlet static pressure are set to zero for the simulation of transient operation of the pump (Koombua *et al*. 2008; Su and Pidaparti 2010). No-slip boundary condition is applied at walls.

### 4.1. Mesh Independence Study

The evaluation of independency of the results from the computational grid is performed by minimizing the maximum element size at boundaries. The mesh independence study was accomplished for steady state flows. Since the largest changes of geometry and flow gradient occurs at the interface of the first and second chambers (section C in Fig. 5a), this section is selected to evaluate grid independency of the simulation.

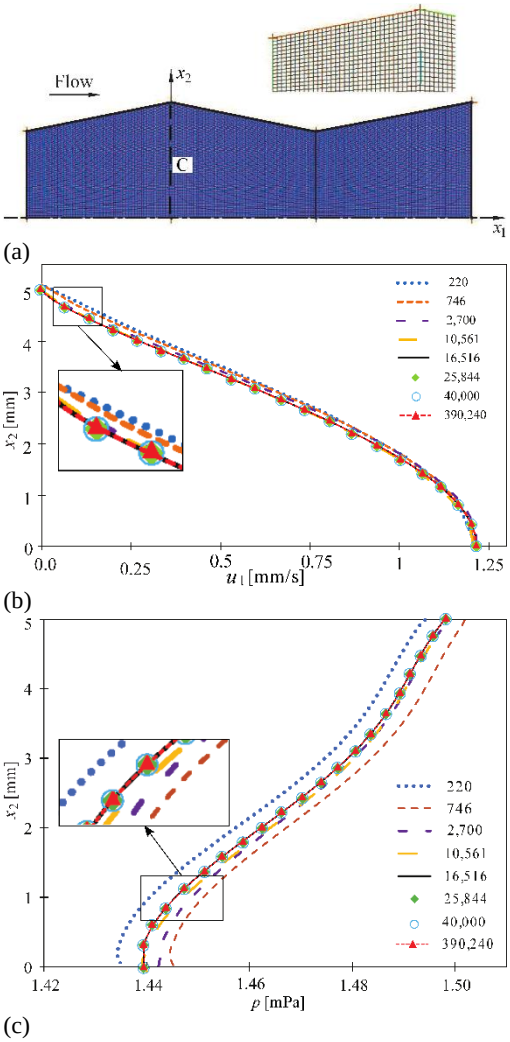


**Fig. 5. (a) Computational grid, (b) and (c) $u_1$ velocity component and pressure distributions along section C at different number of grid cells, respectively. The enlarged segments show the matching of curves for 16,516 and higher grid cells in both velocity, $u_1$, and pressure, $p$, diagrams.**

Figure 5a illustrates a sample computational grid. The distribution of the $x_1$-component of velocity is shown in Fig. 5b, and Fig. 5c illustrates pressure distribution along this section. The results indicate that while the graphs are consistent, the velocity distribution of flow for the last five grids and the pressure distribution for the last four grids are approximately the same. The quantitative representation of the $x_1$-component of velocity and pressure distributions are given in Tab. A.1 in Sec. A. The relative error is defined as

$$\varepsilon = 100\frac{|\varphi - \varphi_{\text{ref}}|}{\varphi_{\text{ref}}} \tag{4}$$

in which $\varphi$ is a typical variable such as pressure $p$ or velocity $u_1$ and $\varphi_{\text{ref}}$ is its reference value as indicated in Tables A.1 and A.2 in Sec. A. This study indicates that the simulation results are independent of the computational grid for a grid with 16,516 cells or higher, and for larger number of grid cells show less than 2.6% relative error. In order to establish a higher level of reliability, a grid of 40,000 cells is used to evaluate the performance of the micropump. This computational grid is fine enough to provide mesh independence and required accuracy for the computation of the flow field parameters.

### 4.2. Time Step Independence Study

The time step independence study of the simulation is performed at seven time steps for a grid with 40,000 cells, for two supply and pump modes during ten working cycles. Table 1 shows the time step values used to evaluate the time step independence of the simulation.

Figure 6 illustrates the distribution of the $u_1$ velocity component at section C (in Fig. 5a) in two supply and pump modes for different time steps and at the membrane frequency of 100 Hz at the tenth cycle of simulation. Based on the results, the velocity distribution of flow at section C in both supply and pump modes is approximately the same for the last five time step values and the graphs are consistent with a relative error less than 2%. The relative error is calculated with reference to the baseline time step 10 μs. The quantitative representation of the $u_1$ velocity component at section C in the supply and pump modes for different time steps are given in Table A.2. This study indicates that the results of the simulation are independent from time step for the

**Table 1 Time steps used in time step independence study**

| Case Number | Time Step [ μs ] |
|---|---|
| 1 | 500 |
| 2 | 250 |
| 3 | 125 |
| 4 | 62.5 |
| 5 | 31.2 |
| 6 | 10 |
| 7 | 1 |

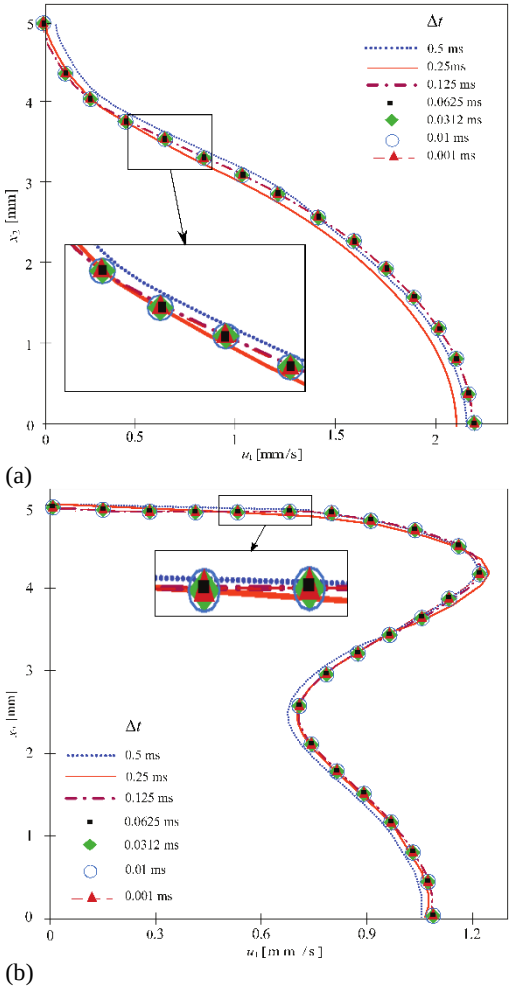


**Fig. 6. $u_1$ velocity component distribution diagram at section C of the micropump chamber for different time steps in, (a) pump mode, (b) supply mode. The enlarged segments show a good match of velocity curves for time steps 0.0625 ms and higher in both diagrams.**

time step of 62.5 μs. In order to establish a higher reliability of the simulation, a time step of 10 μs is selected for the simulation of the hydrodynamic performance of the micropump. This time step is small enough to display all physical changes in the flow field during simulation and gives acceptable results to solve in all examined frequencies below 100 Hz.

### 4.3. Validation

To validate the numerical simulation, a micropump with geometric characteristics in Table 2 is modeled (Koombua *et al*. 2008). The transient response of the

**Table 2 Geometric dimensions of the micropump. Dimensions are in mm**

| $D$ | $L$ | $W_{in}$ | $L_1$ | $W_1$ | $L_2$ | $W_2$ | $L_3$ | $W_{out}$ |
|---|---|---|---|---|---|---|---|---|
| 0.05 | 20 | 2.5 | 9 | 5 | 5.5 | 3.75 | 5.5 | 5 |

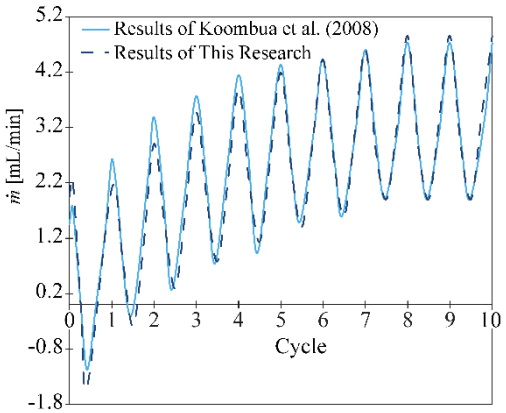


**Fig. 7. Transient mass flow rate over 10 cycles.**

net output mass flow rate at the micropump outlet over the first 10 pump cycles are shown in Fig. 7 for the frequency of 100 Hz, the maximum membrane displacement of 1 mm, and zero differential pressure between inlet and outlet of the pump.

The investigated micropump design by Koombua *et al.* (2008) is based on the fabricated PDMS micropump by Cartin *et al.* (2008) for microfluidic applications. A comparison of this simulation with the work of Koombua *et al.* (2008) indicates that the net output mass flow rate in both cases reaches quasi-steady operating conditions after eight cycles. The maximum mass flow rate through the micropump outlet cross section is 4.8 mL/min, which shows less than 2% relative error.

## 5. RESULTS AND DISCUSSION OF NUMERICAL SIMULATION

In order to evaluate the flow pattern, the fluid velocity fields inside the micropump in both pump and supply modes are presented in Fig. 8 for an actuator frequency of 100 Hz, maximum membrane displacement of 1 mm, and zero differential pressure between inlet and outlet. The movement of the walls is defined by Eq. (3). During each cycle, the movement of the micropump membrane causes periodic changes in fluid volume and pressure, and the flow pattern changes alternately by movement of the membranes. When the micropump is at pumping mode, Fig. 8a, the third membrane expands and the volume of chamber is maximized. On the other hand, the first and second membranes contract, and their corresponding volumes are minimized. Therefore, the volume of stored fluid in the first and second chambers is transferred to the third chamber, and is driven out of the pump.

When the first membrane moves downward, upstream fluid is sucked into the pump and the discharge velocity decreases. Partial reverse flows are visible at inlet and outlet in the pumping mode. However, most of the flow is in the correct direction from inlet to outlet, which shows the micropump can pump the flow in its expected direction. When the micropump is in the supply mode, Fig. 8b, the first and second membranes of the micropump are expanded away from its center line and the flow is

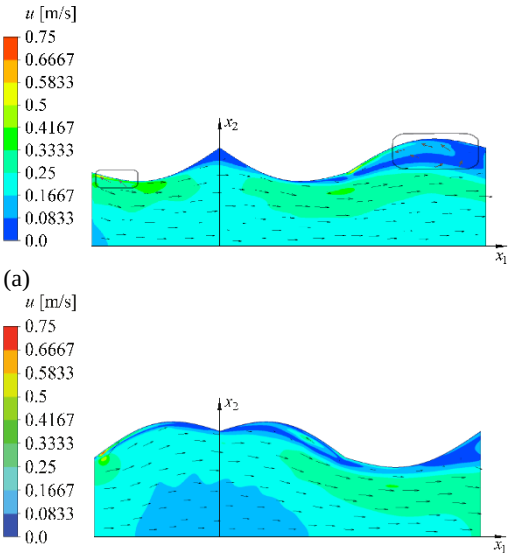


**Fig. 8. Flow field inside the micropump during, (a) pumping mode, and (b) supply mode operation. The boxed regions indicate partial reverse flow.**

drawn in. At the same time, the third membrane contracts and approaches to the central line of the micropump and the fluid is pushed out.

The instantaneous ( $\dot{m}$ ) and mean ( $\bar{\dot{m}}$ ) net mass flow rates

$$\dot{m} = \rho D \int_0^{Y_k} u_1 dx_2 \tag{5}$$

$$\bar{\dot{m}} = \frac{1}{T}\int_t^{t+T} \dot{m} dt \tag{6}$$

at the outlet ($Y_k$=$W_{out}$) and inlet ($Y_k$=$W_{in}$) cross-sections for the upper half of the micropump chamber at 100 Hz actuator frequency, maximum membrane displacement of 1 mm, and zero differential pressure between inlet and outlet is shown in Fig. 9. In this diagram, the maximum mass flow rate passing through the outlet and inlet of the micropump increases over time and the periodic flow pattern reaches a steady state after eight complete cycles. Therefore, the micropump pumps the flow toward the outlet and the net mass flow rate at the output is always positive. The maximum net mass flow rates through the outlet and inlet of the micropump are 92.62 mL/min and 220.09 mL/min, respectively. The mean net mass flow rate at the micropump inlet is approximately 51.16 mL/min.

*Reversibility* or the mean reverse mass flow rate ratio at the outlet, $\bar{\varphi}_{ex}$ , is defined as the time average of the reverse mass flow rate to the gross mass flow rate passing through the pump outlet during a complete cycle, Eq. (11), is shown in Fig. 10.

$$\dot{m}^+ = \rho \int_A \max(u_1, 0) dA \tag{7}$$

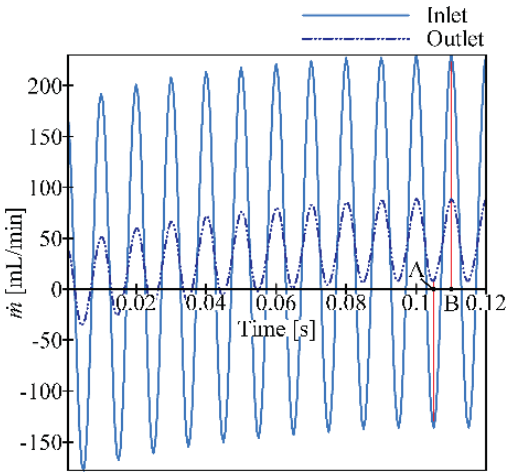


**Fig. 9. Instantaneous net mass flow rate through the inlet and outlet of the micropump.**

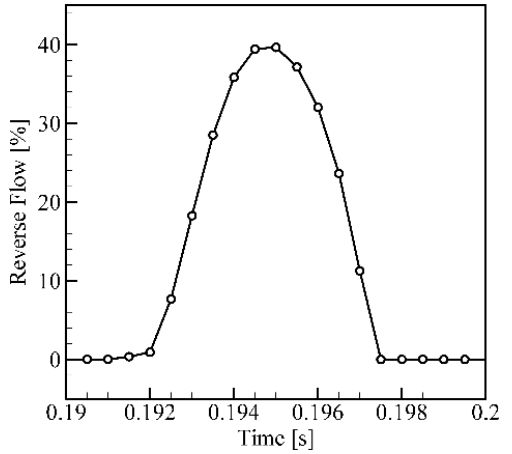


**Fig. 10. Reverse mass flow rate ratio, $\varphi_{ex}$ , vs. time at the outlet of the micropump during one cycle.**

$$\dot{m}^- = \rho \int_A \min(u_1, 0) dA \tag{8}$$

$$\dot{m}^g = |\dot{m}^-| + \dot{m}^+ \tag{9}$$

$$\varphi_{ex} = \frac{|\dot{m}^-|}{\dot{m}^g} \tag{10}$$

$$\bar{\varphi}_{ex} = \frac{1}{T}\int_t^{t+T} \frac{|\dot{m}^-|}{\dot{m}^g} dt \tag{11}$$

where $t$ is time, $A$ is the cross-sectional area at the outlet of the pump, $u_1$ is the velocity component along the $x_1$-axis, $T$ is the common period of forward, $\dot{m}^+$ , and reverse, $\dot{m}^-$ , mass flow rates, and $\varphi_{ex}$ is the reverse mass flow rate ratio. The sum of the absolute values of the forward and reverse mass flow rates is defined as *gross mass flow rate* and indicates the total mass flow rate passing the outlet boundary of

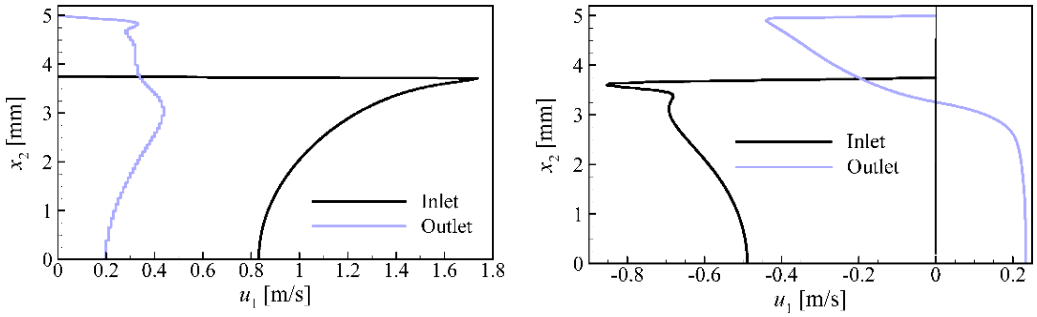


**Fig. 11.** $u_1$ **velocity profile along the** $x_2$ **axis corresponding to (a) maximum (point B in Fig. 9) and (b) minimum (point A in Fig. 9) net mass flow rates at the inlet and outlet of the micropump.**

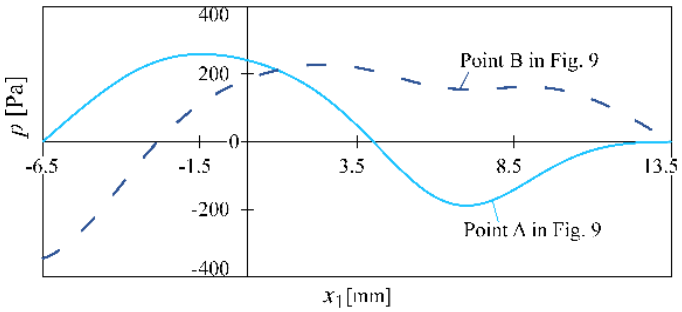


**Fig. 12. Pressure distribution along the centerline (**$x_2$**=0) for the maximum (point B in Fig. 9) and minimum (point A in Fig. 9) inlet and outlet mass flow rates.**

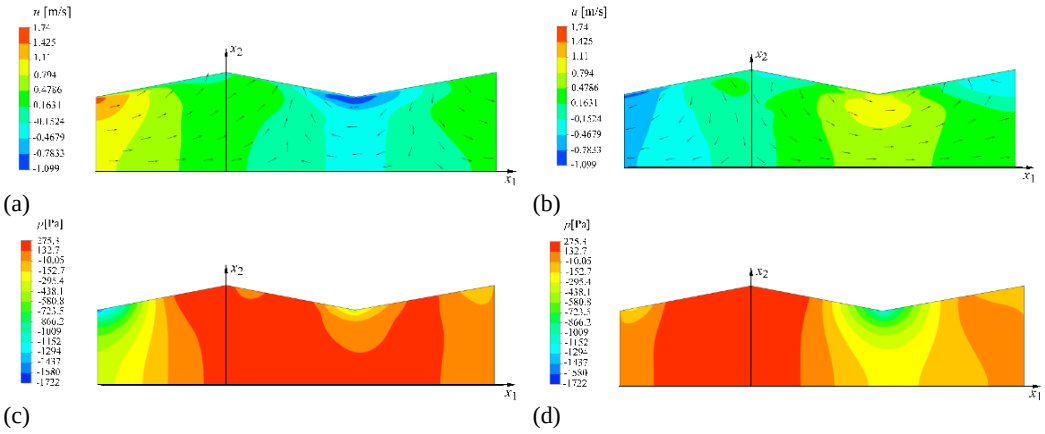


**Fig. 13. (a) Velocity contours corresponding to the maximum inlet and outlet mass flow rates (point B in Fig. 9), (b) velocity contours corresponding to the minimum inlet and outlet mass flow rates (point A in Fig. 9), (c) pressure contours corresponding to the maximum inlet and outlet mass flow rates (point B in Fig. 9), and (d) pressure contours corresponding to the minimum inlet and outlet mass flow rates (point A in Fig. 9).**

the pump. The ratio of the absolute value of the reverse mass flow rate to the gross mass flow rate is defined as *reverse mass flow rate ratio*, $\varphi_{ex}$, and its time mean is defined as *reversibility*, $\overline{\varphi}_{ex}$. Figure 10 shows a typical the reverse mass flow rate ratio for which the reversibility at the micropump outlet is 13.4%.

Velocity and pressure variations along $x_2$ and $x_1$ axes as well as velocity and pressure contours corresponding to minimum (point A in Fig. 9) and maximum (point B in Fig. 9) mass flow rates are shown in Figs 11, 12, and 13. Considering the dynamics of the membranes and fluid flow, the change of the flow variables near the membrane walls are intense. As shown in Figs. 11a and 11b the absolute value of velocity at the inlet and outlet of the micropump is maximum near the membrane and decreases and becomes uniform when approaching the central line of the micropump. Figs. 13a and 13b illustrate that the velocity contours have an intense gradient near the membrane. The movement of the membrane during each cycle changes the direction of the velocity vector, which is seen at the inflection point and the change of direction of the velocity in Fig. 11b. These characteristics are shown in Fig. 13b as reverse flows at the inlet and outlet of the micropump.

**Table 3 Micropump geometric parameters**

| Parameter | Number of levels | Range [ mm ] |
|---|---|---|
| $W_{in}$ | 3 | 2.5 – 5 |
| $W_{out}$ | 3 | 2.5 – 5 |
| $W_1$ | 3 | 2.5 – 5 |
| $W_2$ | 3 | 2.5 – 5 |
| $L_1$ | 3 | 4 – 9 |
| $L_3$ | 3 | 4 – 7 |

The pressure contours corresponding to the maximum inlet and outlet mass flow rates (point B in Fig. 9) show that the pressure at the inlet and outlet of the micropump is non-zero and zero, respectively (Fig. 13c). Also the pressure contours corresponding to the minimum inlet and outlet mass flow rates (point A in Fig. 9) show that the pressure at the inlet and outlet of the micropump is zero (Fig. 13d). These characteristics are shown in Fig. 12.

## 6. Optimization of Micropump

To optimize the performance of the pump the DOE method is used in order to maximize the mean net outlet mass flow rate and minimize reversibility by modifying the geometry of the micropump. Design of Experiment technique helps the designer to limit the calculations needed to find the effects of input variables on output variables. In this method the shortcoming of inaccuracy of using an approximating function is compensated by reducing the number of calculations. A combination of mathematical and statistical methods are used for constructing the design space in which all variants of model are evaluated (Montgomery 2017; Mojaddam and Pullen 2019).

### 6.1. Creating the Design Space

Design space consists of all combinations of parameter values that are chosen to evaluate their effects on the objective functions. There are various methods for creating a design space including the full factorial and the Taguchi methods. When creating the design space by the full factorial method for $n$ parameters, each at $K$ levels, $K^n$ design points are generated (Mason *et al.* 2003; Mojaddam and Pullen 2019). The geometrical parameters of the micropump to create the design space are given in Table 3.

In order to design micropumps with different geometries, the overall length of the micropump chamber and its depth are kept constant at 20 mm and 1 mm, respectively. At each level the variables $W_{in}$, $W_{out}$, $W_1$, $W_2$, $L_1$ and $L_3$ are increment by fifty percent of their ranges. With these 6 parameters each at 3 levels, the full factorial method generates 729 design points, which is inefficient in terms of required computational power and cost.

To reduce the computational cost of optimization, in this study the Taguchi method (Taguchi 1987) is used to create an efficient design space with reasonable number of design points to reduce the number of design points. In Taguchi design method, the number of design points is decreased by using orthogonal arrays and all of the available variables are covered. The Taguchi method generates $N$ design points with $n$ parameters each at $K$ levels using $L_N(K^n)$ orthogonal arrays (Byrne and Taguchi 1987). These points are selected from the total number of design points in the full factorial method. The members of the set exist exactly once in each row and once in each column without repetition (Kackar 1985; Taguchi 1987). The Taguchi method provides 27 design points for the micropump, with 6 parameters each in 3 levels.

### 6.2. Results and Discussion of Optimization

Based on the results of the Taguchi method, different configurations are generated and simulated. 27 design configurations used for the optimization of the micropump are shown in Fig. 14. All models are examined under the same conditions, i.e. membranefrequency of 100 Hz, maximum membrane displacement of 1 mm, and zero differential pressure between inlet at outlet. Figure 15 shows the mean net outlet mass flow rate and reversibility. The values are scaled by their corresponding values of a baseline micropump configuration, model 9 in Fig. 14.

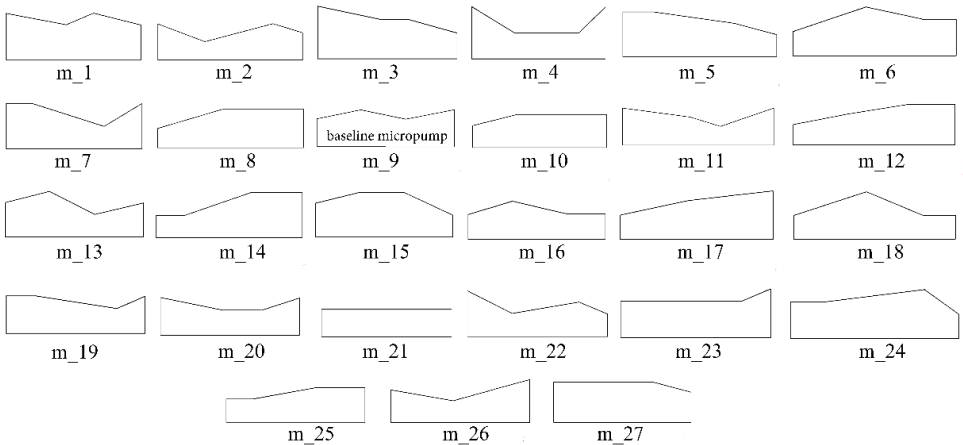


**Fig. 14. Different configurations of the micropump by Taguchi method.**

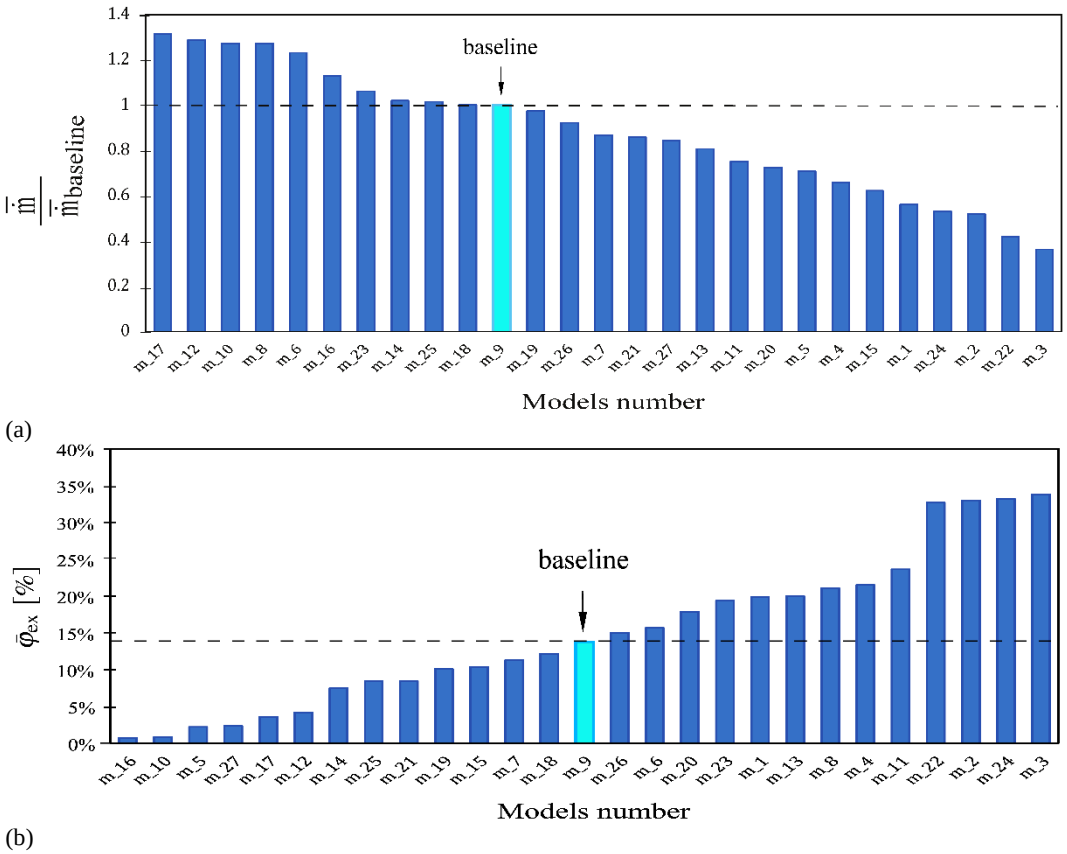


**Fig. 15. (a) Mean net outlet mass flow rate, and (b) reversibility at the outlet for 27 micropump configurations during one cycle.**

The highest mean net outlet mass flow rates are 67.69 mL/min, 66.29 mL/min, and 65.53 mL/min for models 17, 12, and 10, respectively. The results show that in the configurations where the micropump inlet width is the smallest and the micropump outlet width is the largest, Fig. 14, when the outlet width is greater than or equal to the width of second median throat and the inlet width of micropump is less than the width of first median throat, the mean net outlet mass flow rate can have the maximum value, Fig. 15.

The lowest reversibility of the micropump at outlet for models 16, 10 and 5 are 0.69%, 0.79% and 2.19%, respectively. Therefore, in the geometry when the width of the first median throat is greater than or equal to the inlet width of micropump and the width of the second median throat is less than or equal to the width of the first median throat and the outlet width is less than or equal to the width of the first and second median throats, the reversibility can be the smallest, Figs. 14 and 15.

As shown in Fig. 15, the lowest reversibility does not necessarily occur at the highest mean net outlet mass flow rate. Similarly, the lowest mean net outlet mass flow rate does not necessarily happen at the highest reversibility. This shows how the mean net outlet mass flow and reversibility are affected by other parameters. For example, models 17 and 12 have the highest mean net outlet mass flow rate, while the lowest reversibility is related to models 16 and 10. Therefore, models 17 and 16 can be considered for the highest mean net outlet mass flow rate and the lowest reversibility at the micropump outlet, respectively. As shown in Fig. 15, among the models designed for the micropump in the present study, models 17, 12, 10, and 16 present superior performances.

Based on the comparison of the models and examining the performance of the micropumps, choosing an appropriate model for the micropump design, depends on its application. When the micropump is intended only to transfer fluid, an amount of reversibility can be accepted in favor of increased net mass flow rate. On the other hand in most medical applications, where the integrity of fluid components (e.g. blood cells) is likely to be affected by excessive shear stress in the flow field, it is important to have minimum reverse flow back into the pump.

### 6.3. Effective Parameter Identification

The scatter plot for all models is illustrated in Fig. 16. The graph shows the relation between the input and output variables, as well as the degree of impact of an input variable on an output variable. In the following diagram, Pearson correlation coefficient (P-c), is used to calculate the degree and the amount of linear relation between the input and output variables. When the Pearson correlation coefficient is closer to +1, there is a direct and positive relation between input and output variables. When this

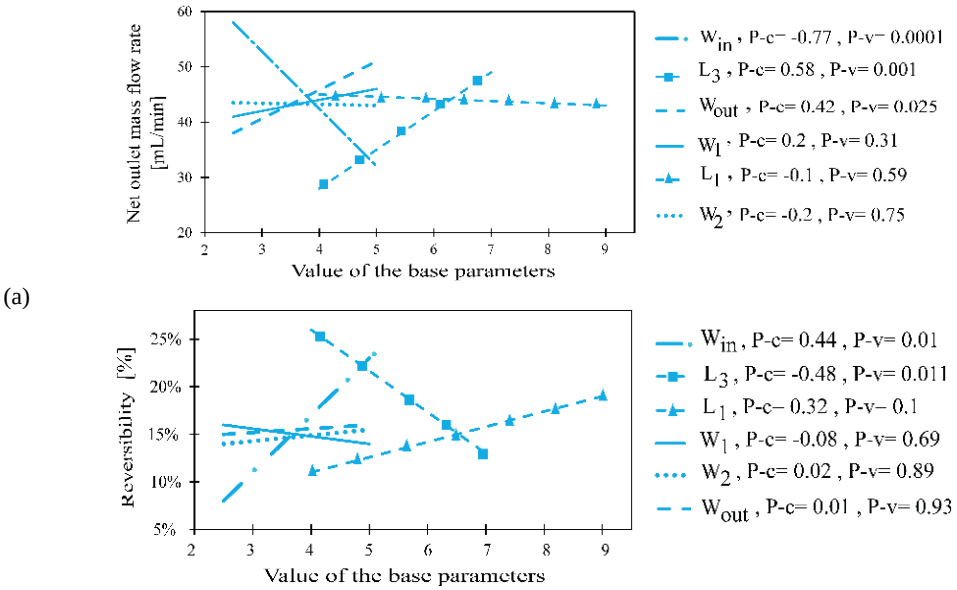


**Fig. 16. Scatter plot of the effect of geometric parameters on objective functions, (a) mean net outlet mass flow rate, (b) reversibility.**

coefficient is close to -1, it shows the opposite or negative relation between the two input and output variables (Lee Rodgers and Nicewander 1988). The P-value (P-v) indicates the effect of an input variable on the output variable. If the P-value is less than 0.05, the input variable has a significant effect on the output variable. However, if its value is greater than 0.05, it shows negligible effect of the input variable on the output variable (Montgomery, 2017).

As displayed in Fig. 16a, the half of the inlet width, $W_{in}$, the length of the third membrane, $L_3$, and the half of the output width, $W_{out}$, are the main parameters in determining the mean net outlet mass flow rate. These three parameters have the highest slope and, therefore, the highest impact on the mean net outlet mass flow rate. The half-width of the first throat, $W_1$, has medium effect. The mean net outlet mass flow rate remains almost consonant when changing the length of the first membrane, $L_1$, and the half-width of the second throat, $W_2$. Therefore, their effects are negligible. However, in a given range the mean net outlet mass flow rate relies on $W_{out}$, $W_1$, and $L_3$, and is inversely related to $W_{in}$.

As displayed in Fig. 16b, the three parameters $W_{in}$, $L_3$, and $L_1$ are the main parameters in determining the reversibility and have the highest slope and impact on the other parameters. $W_1$, $W_2$, and $W_{out}$ have slight effect on the reversibility. As shown in Fig. 16b, in a given range the value of reversibility relies on $W_{in}$, $W_{out}$, $W_2$ and $L_1$ and is inversely related to $W_1$ and $L_3$.

## 6.4. Response Surface Method (RSM)

The simultaneous impact of geometric parameters on the objective function can be obtained using the response surface method. RSM is constructed as a substitute model based on the most important effects of input variables on the outputs (Montgomery and Runger 2010). A second-order polynomial model, Eq. (12), is used to find the relation between the objective function (mean net outlet mass flow rate and reversibility) and the independent input variables (the geometric parameters).

$$y = \alpha_0 + \sum_{i=1}^{k} \alpha_i x_i + \sum_{\substack{i=1 \\ i<j}}^{k} \sum_{j=1}^{k} \beta_{ij} x_i x_j + \sum_{i=1}^{k} \beta_{ii} x_i^2 + \grave{o} \tag{12}$$

where $x_i$ represent independent input variables ($i, j = 1, 2, \ldots, k$), $y$ is the output variable, $\alpha$ and $\beta$ represents the constant coefficients of the parameters and $\epsilon$ is the regression error. This equation indicates how the value of objective function changes by each of the independent input variables as well as their impact on the performance of objective function (Myers *et al.* 2004; Khuri and Mukhopadhyay 2010; Namazizadeh *et al.* 2020).

Several parameters can simultaneously affect the objective functions. Figure 17 displays the sensitivity of the objective functions, i.e. the mean net outlet mass flow rate and the reversibility, to the geometrical parameters using the Pareto diagram at the outlet of the micropump. The horizontal axis in diagram indicates the effect of geometric parameters on the objective function. Considering the mean net outlet mass flow rate, $L_3^2$, $L_3W_1$, and $W_{out}$ have the most effects, and $L_1^2$ and $W_{out}^2$ have the least effects, Fig. 17a. $L_3^2$ is considered as the most effective one in determining the reversibility, while $W_1^2$ and $W_{out}^2$ have the least impact, Fig. 17b.

## 6.5. Finding the Optimal Geometry

Based on the above mentioned analysis, the fitness

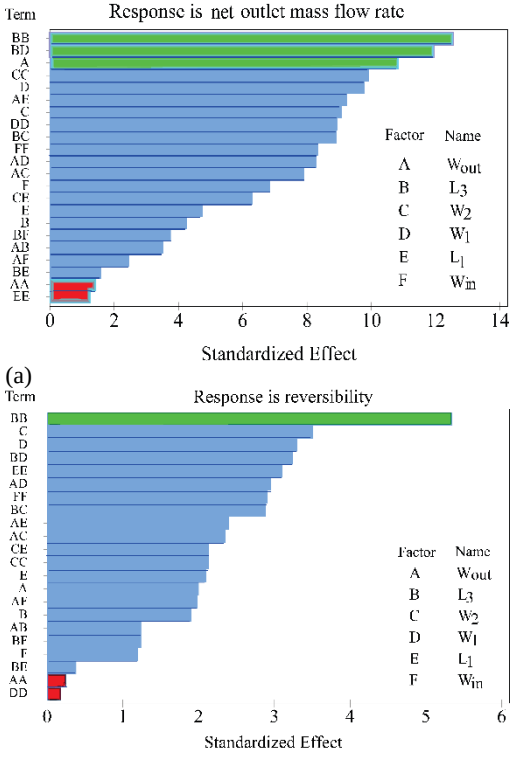


**Fig. 17. Pareto chart of the sensitivity of the objective functions, (a) mean net outlet mass flow rate and (b) reversibility to geometric parameters.**

function, Eq. (12), is extracted and optimized for objective functions to find the independent input variables ($W_{in}$, $W_{out}$, $W_1$, $W_2$, $L_1$, $L_3$), maximize the mean net outlet mass flow rate, and minimize the reversibility. An iterative procedure is used to maximize the mean net outlet mass flow rate and minimize the reversibility. In this procedure, independent input variables are changed in a given interval in each repetition and the objective functions are updated. This process is continued until the optimum geometry is obtained for the maximum mean net outlet mass flow rate and minimum reversibility separately. The optimized geometries and their dimensions for the maximum mean net outlet mass flow rate and minimum reversibility are shown in Figs. 18a and 18b, respectively.

The results of the initial models, the optimal models, and model of the Koombua *et al.* (2008) are reported in Table 4 and Fig. 19. The maximum of mean net outlet mass flow rate and minimum reversibility corresponding to the optimum geometries are 95.82 mL/min and 0.05%, respectively. The optimal model for the mean net outlet mass flow rate compared to the initial model and the Koombua *et al.* (2008) model show approximately 1.855 and 1.344 times increase in mass flow rate, respectively.

In the optimal model for mass flow rate, the mean net outlet mass flow rate is maximum and the reversibility is significantly reduced compared to the initial and Koombua *et al.* (2008) models. The optimum model for the reversibility compared to the

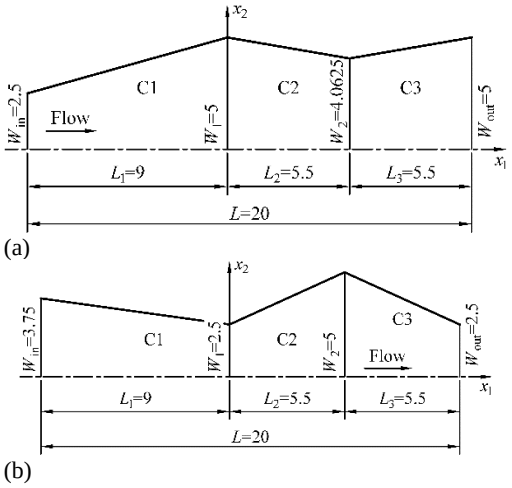


**Fig. 18. Dimensions of optimal micropumps for (a) maximum mean net outlet mass flow rate and (b) minimum reversibility. Only the upper half of the micropump chamber is shown. Dimensions are in mm.**

**Table 4 Comparison of reference and optimized micropumps**

| Micropump model | $\bar{\dot{m}}\left[\frac{\text{mL}}{\text{min}}\right]$ | $\bar{\varphi}_{ex}$ [%] |
|---|---|---|
| Initial model | 51.64 | 13.74 |
| Koombua et al. (2008) model | 71.26 | 2.59 |
| Optimal model for mass flow rate | 95.82 | 1.53 |
| Optimal model for reversibility | 39.29 | 0.05 |

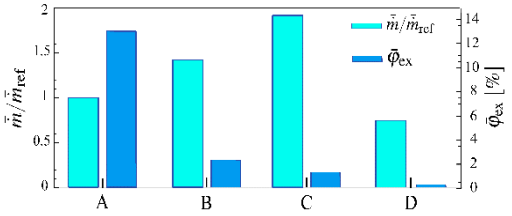


**Fig. 19. Mean net outlet mass flow rate and reversibility at the outlet of the micropump with a depth of 1 mm during one cycle. A: initial model, B: Koombua *et al.* (2008) model, C: optimal mass flow rate, D: optimal reversibility model.**

initial and Koofinmbua *et al.* (2008) models represents 13.69% and 2.54% less reversibility, respectively,Fig. 19. Based on the above analysis and reported results in previous studies (Cartin *et al.* 2008; Su and Pidaparti 2010) although the Koombua *et al.* (2008) model is used as an optimal model for nozzle-diffuser piezoelectric micropumps, the introduced optimum models in this paper offer an improvement of 34.5% for the mean net outlet mass flow rate and 98% for the reversibility compared to the Koombua *et al.* (2008) model.

## 7. CONCLUSION

This study presents optimal configurations for a nozzle-diffuser micropump with oscillating membranes using the DOE method and dynamic mesh simulation. Six independent geometrical

parameters are considered to design micropump. The Taguchi analysis method is used to create an efficient design space, and the mean net outlet mass flow rate and reversibility are obtained for each model by numerical simulation. Second-order polynomials are used to form response surfaces, and the most effective parameters in determining target performance are identified. Then, the objective functions are used to optimize the pump and two optimal geometries are proposed for maximum mean net outlet mass flow rate and minimum reversibility at the micropump outlet. The resulting models demonstrated an improvement of 34.5% for the mean net outlet mass flow rate and 98% for the reversibility compared to the optimum model with the same chamber depth.

## ACKNOWLEDGEMENTS

The support and resources from the Center for High Performance Computing (SARMAD) at the Shahid Beheshti University are acknowledged.

## REFERENCES

Abhari, F., H. Jaafar and N. A. Md Yunus (2012). A comprehensive study of micropumps technologies. *International Journal of Electrochemical Science* 7 (10), 9765-9780.

Byrne, D. M. and S. Taguchi (1987). The Taguchi approach to parameter design. *Quality Progress* 20 (12),19-26.

Cartin, C. P., R. M. Pidaparti and G. M. Atkinson (2008). Design and fabrication of a PDMS micropump with moving membranes. In *2008 17th Biennial University/Government/ Industry Micro/Nano Symposium*, IEEE.

Cui, Q., C. Liu and X. F. Zha (2008). Simulation and optimization of a piezoelectric micropump for medical applications. *The International Journal of Advanced Manufacturing Technology* 36(5–6), 516-524.

Currie, I. G. (2016). *Fundamental Mechanics of Fluids*. CRC Press.

He, X., S. C. Cai, Z. D. Deng and S. Yang (2017). Experimental and numerical study of flow characteristics of flat-walled diffuser/nozzles for valveless piezoelectric micropumps. *Proceedings of the Institution of Mechanical Engineers, Part C: Journal of Mechanical Engineering Science* 231 (12), 2313-2326.

Issa, R. I. (1986). Solution of the implicitly discretised fluid flow equations by operatorsplitting. *Journal of Computational Physics* 62, 40-65.

Iverson, B. D. and S. V. Garimella (2008). Recent advances in microscale pumping technologies: a review and evaluation. *Microfluidics and Nanofluidics* 5(2), 145-174.

Kackar, R. N. (1985). Off-line quality control, parameter design, and the Taguchi method. *Journal of Quality Technology* 17(4),176-188.

Karimi, S., P. Mehrdel, J. Farré-Lladós and J. Casals-Terré (2019). A passive portable microfluidic blood–plasma separator for simultaneous determination of direct and indirect ABO/Rh blood typing. *Lab on a Chip* 19, 3249-3260.

Karimi, S., M. Mojaddam, S. Majidi, P. Mehrdel, J. Farré-Lladós and J. Casals-Terré (2021). Numerical and experimental analysis of a high-throughput blood plasma separator for point-of-care applications. *Analytical and Bioanalytical Chemistry* 413, 2867-2878.

Khuri, A. I. and S. Mukhopadhyay (2010). Response surface methodology. *Wiley Interdisciplinary Reviews: Computational Statistics* 2(2), 128-149.

Kim, Y. S., J. H. Kim, K. H. Na and K. Rhee (2005). Experimental and numerical studies on the performance of a polydimethylsiloxane valveless micropump. *Proceedings of the Institution of Mechanical Engineers, Part C: Journal of Mechanical Engineering Science* 219(10), 1139-1145.

Koombua, K., R. M. Pidaparti and G. M. Atkinson (2008). Microfluidic simulations of micropump with multiple vibrating membranes. In *Proceedings of the 11th International Conference on Modeling and Simulation of Microsystems, Boston, MA*.

Koombua, K. and R. M. Pidaparti (2010). Performance evaluation of a micropump with multiple pneumatic actuators via coupled simulations. *Engineering Applications of Computational Fluid Mechanics* 4(3),357-364.

Kumar, C. S. S. R. (2010). *Microfluidic devices in nanotechnology: applications*. John Wiley & Sons.

Lee Rodgers, J. and W. A. Nicewander (1988). Thirteen ways to look at the correlation coefficient. *The American Statistician* 42(1), 59-66.

Li, Z. and X. Zheng (2017). Review of design optimization methods for turbomachinery aerodynamics. *Progress in Aerospace Sciences* 93, 1-23.

Mason, R. L., R. F. Gunst and J. L. Hess (2003). *Statistical Design and Analysis of Experiments: With Applications to Engineering and Science*. John Wiley & Sons.

Mojaddam, M. and K. R. Pullen (2019). Optimization of a centrifugal compressor using the design of experiment technique. *Applied Sciences* 9(2), 291.

Montgomery, D. C. and G. C. Runger (2010). *Applied Statistics and Probability for Engineers*. John Wiley & Sons.

Montgomery, D. C. (2017). *Design and Analysis of Experiments*. John wiley & sons.

Myers, R. H., D. C. Montgomery, G. G. Vining, C. M. Borror and S. M. Kowalski (2004). Response surface methodology: a retrospective and literature survey. *Journal of Quality Technology* 36(1), 53-77.

Namazizadeh, M., M. Talebian Gevari, M. Mojaddam and M. Vajdi (2020). Optimization of the splitter blade configuration and geometry of a centrifugal pump impeller using design of experiment. *Journal of Applied Fluid Mechanics* 13(1), 89-101.

Noruz Shamsian, O., A. Mohseni and M. Mojaddam (2020). Design of a microseparator for circulating tumor cells (CTCs) from blood flow using hybrid pinched flow fractionation (PFF) and dielectrophoresis methods. *Journal of Solid and Fluid Mechanics* 10(1), 281-296. (in Persian).

Ohnstein, T., T. Fukiura, J. Ridley and U. Bonne (1990). Micromachined silicon microvalve. In *IEEE Proceedings on Micro Electro Mechanical Systems, An Investigation of Micro Structures, Sensors, Actuators, Machines and Robots*.

Patankar, S. V. and D. B. A. Spalding (1972). Calculation procedure for heat, mass and momentum transfer in three-dimensional parabolic flows. *International Journal of Heat and Mass Transfer* 15, 1787-1806.

Piterah, N. S. M., N. R. Ong, M. H. A. Aziz, J. B. Alcain, W. M. W. N. Haimi and Z. Sauli (2017). Investigation of micropump mechanism for medical application (blood transport application). In *AIP Conference Proceedings, volume 1885, page 020299 (5pp).*

Saggere, L. (2015) Membrane actuation for micropumps. In Li, Dongqing, (Ed.), *Encyclopedia of Microfluidics and Nano-fluidics*, pages 1741–1746. Springer US,

Sateesh, J., K. G. Sravani, R. A. Kumar, K. Guha and K. S. Rao (2018). Design and flow analysis of MEMS based piezo-electric micro pump. *Microsystem Technologies* 24(3), 1609-1614.

Shoji, S., S. Nakagawa and M. Esashi (1990). Micropump and sample-injector for integrated chemical analyzing systems. *Sensors and Actuators A: Physical* 21(13), 189-192.

Smits, J. G. (1990). Piezoelectric micropump with three valves working peristaltically. *Sensors and Actuators A: Physical* 21(13), 203-206.

Stemme, E. and G. Stemme (1993). A valveless diffuser/nozzlebased fluid pump. *Sensors and Actuators A: Physical* 39(2), 159-167.

Su, G. and R. M. Pidaparti (2010). Transport of drug particles in micropumps through novel actuation. *Microsystem Technologies* 16(4), 595-606.

Taguchi, G. (1987). Engineering methods to optimize quality and minimize costs. *System of Experimental Design* 1, 1-85.

Verma, P., D. Chatterjee and T. Nagarajan (2009). Design and development of a modular valveless micropump on a printed circuit board for integrated electronic cooling. *Proceedings of the Institution of Mechanical Engineers, Part C: Journal of Mechanical Engineering Science* 223(4), 953-963.

Yamahata, C., C. Lotto, E. Al-Assaf and M. A. M. Gijs (2005). A PMMA valveless micropump using electromagnetic actuation. *Microfluidics and Nanofluidics* 1(3),197-207.

Yao, J., G. R. Liu, D. Qian, C. L. Chen and G. X. Xu (2013). A moving-mesh gradient smoothing method for compressible CFD problems. *Mathematical Models and Methods in Applied Sciences* 23(2), 273-305.

Yao, Q., D. Xu, L. S. Pan, A. L. Melissa Teo, W. M. Ho, V. S. Peter Lee and M. Shabbir (2007). CFD simulations of flows in valveless micropumps. *Engineering Applications of Computational Fluid Mechanics* 1(3), 181-188.

Yazdani, A. and A. Mohseni (2017). Three-dimensional aerothermodynamic optimization of the stator blade of an axial-flow gas turbine in an open-source platform. *Modares Mechanical Engineering* 17(10), 176-184. (in Persian).

Zahn, J. D. (2015). Integrated microdevices for medical diagnostics. In Li, Dongqing (ed.) *Encyclopedia of Microfluidics and Nanofluidics*, pages 1411– 1418. Springer New York.

Zengerle, R. and M. Richter (1994). Simulation of microfluid systems. *Journal of Micromechanics and Microengineering* 4(4), 192.

Zhu, M., P. Kirby, M. Wacklerle, M. Herz and M. Richter (2009). Optimization design of multimaterial micropump using finite element method. *Sensors and Actuators A: Physical* 149(1),130-135.

## A. TABLES

**Table A.1. Values of $u_1$ velocity component and pressure along section C in Fig. 5 for different number of grid cells.**

| Number of Grid Cells | $x_2$ [mm] | $u_1$ [mm/s] | $p$ [mPa] | $\varepsilon_{u_1}$ [%] | $\varepsilon_p$ [%] |
|---|---|---|---|---|---|
| 220 | 0.51 | 1.177 | 1.433 | 1.506 | 0.486 |
| | 1.79 | 0.978 | 1.451 | 0.407 | 0.480 |
| | 3.07 | 0.608 | 1.473 | 2.184 | 0.472 |
| | 4.35 | 0.189 | 1.485 | 2.588 | 0.469 |
| 746 | 0.51 | 1.188 | 1.448 | 0.585 | 0.5 |
| | 1.79 | 0.978 | 1.466 | 0.407 | 0.548 |
| | 3.07 | 0.594 | 1.487 | 0.168 | 0.472 |
| | 4.35 | 0.155 | 1.499 | 0.649 | 0.469 |
| 2,700 | 0.51 | 1.213 | 1.443 | 1.506 | 0.208 |
| | 1.79 | 0.996 | 1.460 | 1.425 | 0.137 |
| | 3.07 | 0.602 | 1.480 | 1.176 | 0.00100 |
| | 4.35 | 0.154 | 1.492 | 0.00323 | 0.00335 |
| 10,561 | 0.51 | 1.197 | 1.444 | 0.167 | 0.27 |
| | 1.79 | 0.982 | 1.462 | 0.00101 | 0.274 |
| | 3.07 | 0.598 | 1.483 | 0.504 | 0.202 |
| | 4.35 | 0.154 | 1.495 | 0.000647 | 0.201 |
| 16,516 | 0.51 | 1.195 | 1.440 | 102(-4)$^{\dagger}$ | 1.04(-5) |
| | 1.79 | 0.982 | 1.458 | 2.03(-4) | 2.05(-4) |
| | 3.07 | 0.595 | 1.480 | 1.67(-5) | 4.05(-5) |
| | 4.35 | 0.154 | 1.492 | 6.47(-5) | 1.54(-5) |
| 25,844 | 0.51 | 1.195 | 1.440 | 2.51(-5) | 1.11(-5) |
| | 1.79 | 0.982 | 1.458 | 2.03(-5) | 7.67(-6) |
| | 3.07 | 0.595 | 1.480 | 3.35(-5) | 3.44(-5) |
| | 4.35 | 0.154 | 1.492 | 3.23(-6) | 1.54(-5) |
| 40,000 | 0.51 | 1.195$^{\ddagger}$ | 1.440$^{\ddagger}$ | – | – |
| | 1.79 | 0.982$^{\ddagger}$ | 1.458$^{\ddagger}$ | – | – |
| | 3.07 | 0.595$^{\ddagger}$ | 1.480$^{\ddagger}$ | – | – |
| | 4.35 | 0.154$^{\ddagger}$ | 1.492$^{\ddagger}$ | – | – |
| 390,240 | 0.51 | 1.195 | 1.440 | 2.51(-6) | 2.49(-6) |
| | 1.79 | 0.982 | 1.458 | 3.15(-6) | 1.11(-6) |
| | 3.07 | 0.595 | 1.480 | 6.71(-6) | 2.49(-7) |
| | 4.35 | 0.154 | 1.492 | 6.47(-6) | 1.60(-6) |

**Table A.2. $u_1$ velocity component at section C in Fig. 6 in pump and supply modes for different time steps**

| Time Step [ms] | $x_2$ [mm] | $u_1^{\mathrm{PM}}$ [mm/s] | $u_1^{\mathrm{SM}}$ [mm/s] | $\varepsilon_{u_1}^{\mathrm{PM}}$ [%] | $\varepsilon_{u_1}^{\mathrm{SM}}$ [%] |
|---|---|---|---|---|---|
| 0.5 | 0.51 | 2.064 | 1.070 | 2.365 | 0.198 |
| | 1.79 | 1.725 | 0.781 | 3.035 | 3.101 |
| | 3.07 | 1.081 | 0.922 | 4.748 | 3.151 |
| | 4.35 | 0.170 | 1.090 | 40.495 | 0.900 |
| 0.25 | 0.51 | 2.014 | 1.090 | 4.730 | 0.00229 |
| | 1.79 | 1.679 | 0.804 | 5.621 | 0.248 |
| | 3.07 | 0.932 | 0.953 | 9.680 | 0.105 |
| | 4.35 | 0.120 | 1.100 | 0.826 | 0.00290 |
| 0.125 | 0.51 | 2.094 | 1.092 | 0.946 | 0.183 |
| | 1.79 | 1.759 | 0.810 | 1.124 | 0.496 |
| | 3.07 | 1.012 | 0.952 | 1.937 | 0.00441 |
| | 4.35 | 0.100 | 1.100 | 0.826 | 0.00945 |
| 0.0625 | 0.51 | 2.114 | 1.090 | 3.49(-3)$^{\dagger}$ | 1.00(-4) |
| | 1.79 | 1.779 | 0.806 | 2.24(-4) | 1.36(-4) |
| | 3.07 | 1.032 | 0.952 | 4.84(-4) | 8.61(-4) |
| | 4.35 | 0.121 | 1.100 | 1.48(-4) | 1.80(-4) |
| 0.0312 | 0.51 | 2.114 | 1.090 | 1.37(-6) | 1.92(-5) |
| | 1.79 | 1.779 | 0.806 | 1.68(-5) | 1.61(-5) |
| | 3.07 | 1.032 | 0.952 | 2.61(-5) | 1.68(-6) |
| | 4.35 | 0.121 | 1.100 | 8.23(-5) | 3.36(-5) |
| 0.01 | 0.51 | 2.114$^{\ddagger}$ | 1.090$^{\ddagger}$ | – | – |
| | 1.79 | 1.779$^{\ddagger}$ | 0.806$^{\ddagger}$ | – | – |
| | 3.07 | 1.032$^{\ddagger}$ | 0.952$^{\ddagger}$ | – | – |
| | 4.35 | 0.121$^{\ddagger}$ | 1.100$^{\ddagger}$ | – | – |
| 0.001 | 0.51 | 2.114 | 1.090 | 2.78(-6) | 4.58(-6) |
| | 1.79 | 1.779 | 0.806 | 2.85(-6) | 5.08(-7) |
| | 3.07 | 1.032 | 0.952 | 3.87(-7) | 4.09(-6) |
| | 4.35 | 0.121 | 1.100 | 2.14(-7) | 2.18(-6) |